

MIT Open Access Articles

*Evaluation of Long-Term SSM/I-
Based Precipitation Records over Land*

The MIT Faculty has made this article openly available. **Please share** how this access benefits you. Your story matters.

Citation: Alemohammad, Seyed Hamed, Dara Entekhabi, and Dennis B. McLaughlin. "Evaluation of Long-Term SSM/I-Based Precipitation Records over Land." *Journal of Hydrometeorology* 15, no. 5 (October 2014): 2012–2029. © 2014 American Meteorological Society

As Published: <http://dx.doi.org/10.1175/jhm-d-13-0171.1>

Publisher: American Meteorological Society

Persistent URL: <http://hdl.handle.net/1721.1/96896>

Version: Final published version: final published article, as it appeared in a journal, conference proceedings, or other formally published context

Terms of Use: Article is made available in accordance with the publisher's policy and may be subject to US copyright law. Please refer to the publisher's site for terms of use.



Evaluation of Long-Term SSM/I-Based Precipitation Records over Land

SEYED HAMED ALEMOHAMMAD, DARA ENTEKHABI, AND DENNIS B. MCLAUGHLIN

Department of Civil and Environmental Engineering, Massachusetts Institute of Technology, Cambridge, Massachusetts

(Manuscript received 15 October 2013, in final form 14 June 2014)

ABSTRACT

The record of global precipitation mapping using Special Sensor Microwave Imager (SSM/I) measurements now extends over two decades. Similar measurements, albeit with different retrieval algorithms, are to be used in the Global Precipitation Measurement (GPM) mission as part of a constellation to map global precipitation with a more frequent data refresh rate. Remotely sensed precipitation retrievals are prone to both magnitude (precipitation intensity) and phase (position) errors. In this study, the ground-based radar precipitation product from the Next Generation Weather Radar stage-IV (NEXRAD-IV) product is used to evaluate a new metric of error in the long-term SSM/I-based precipitation records. The new metric quantifies the proximity of two multidimensional datasets. Evaluation of the metric across the years shows marked seasonality and precipitation intensity dependence. Drifts and changes in the instrument suite are also evident. Additionally, the precipitation retrieval errors conditional on an estimate of background surface soil moisture are estimated. The dynamic soil moisture can produce temporal variability in surface emissivity, which is a source of error in retrievals. Proper filtering has been applied in the analysis to differentiate between the detection error and the retrieval error. The identification of the different types of errors and their dependence on season, intensity, instrument, and surface conditions provide guidance to the development of improved retrieval algorithms for use in GPM constellation-based precipitation data products.

1. Introduction

From the first launch of the Special Sensor Microwave Imager (SSM/I) on board the Defense Meteorological Satellite Program (DMSP) platforms in 1987, there has been 25 years of continuous monitoring of the earth's atmosphere using this microwave instrument. This includes the launch of the new version of the instrument Special Sensor Microwave Imager/Sounder (SSMIS) as well. [Figure 1](#) shows the timeline of these two instruments in orbit ([Berg et al. 2012](#)). This dataset provides a valuable climatological record that can be used for different applications. However, it is necessary to evaluate the products of these instruments at different spatial and temporal scales to have a better and deeper insight into the quality of the records. Furthermore, the results of this evaluation can help guide improved retrieval algorithms.

There is an increasing need for real-time and near-real-time measurements from satellites to be incorporated into meteorological and hydrological hazards decision support systems. A better quantification of errors in spaceborne instrument data and associated retrievals is important to guide where efforts need to focus in improving data products' algorithms. Currently, there are several multiplatform satellite precipitation products that merge different spaceborne estimates of precipitation together and produce global maps of precipitation over land and oceans ([Huffman et al. 2007](#); [Joyce et al. 2010](#); [Hsu and Sorooshian 2008](#); [Xie et al. 2007](#); [Kubota et al. 2007](#)). All these methods use brightness temperature measurements from infrared instruments in geostationary orbit as their main input since they provide the space-time continuity of measurements within the instrument viewing disc. Mostly, these approaches calibrate their algorithms using the more accurate but less frequently refreshed estimates of precipitation from passive microwave (PMW) instruments such as SSM/I in low Earth orbit as well as gauge measurements. However, there has not been a comprehensive spatial and temporal analysis of the quality of the PMW measurements, especially those from SSM/I and its follow-on instruments. It is thus

Corresponding author address: S. Hamed Alemohammad, Massachusetts Institute of Technology, 77 Massachusetts Ave., MIT Bldg. 48-216, Cambridge, MA 02139.
E-mail: hamed_al@mit.edu

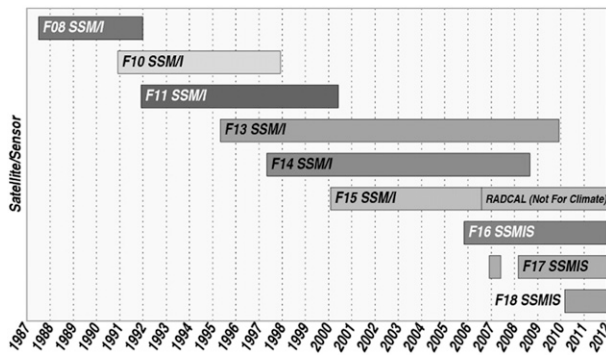


FIG. 1. Timeline of SSM/I and SSMIS instruments in orbit (Berg et al. 2012).

necessary and useful to quantify the uncertainty in the PMW-based retrievals for these merged products.

There is a long history of studies to evaluate the errors associated with PMW-based precipitation estimates. Many of the studies are associated with field campaigns or have limited-duration and limited-coverage domains in their comparisons. Hence, the types of errors such as their dependence on intensity, season, etc. cannot be fully characterized.

During the 1990s, Ferraro and Marks (1995) used the ground-based radar measurements of rainfall over the United States, United Kingdom, and Japan to develop a precipitation retrieval algorithm for SSM/I measurements. They categorized the precipitation into several magnitude bins and provided coefficients for nonlinear fits to the instrument data. They found an error of about 10% for scattering algorithm and 20% for emission algorithm. Although the algorithm has gone through revisions, the original version is still in practice. The SSM/I rain-rate product that is used in the present study is based on this algorithm. Moreover, several operational products that produce global maps of precipitation by merging measurements from different sensors take advantage of the SSM/I rain rate based on the Ferraro and Marks algorithm (Table 1). There have also been several studies that use this algorithm (e.g., Turk et al. 2000; Krishnamurti et al. 2001; Miller et al. 2001; Kidd et al. 2003).

Bell et al. (2001) investigate the monthly average precipitation estimates based on the SSM/I sensor on board *DMSP-F10* and *DMSP-F11*. They apply spatial averaging to form coarse-spatial-resolution $2.5^\circ \times 2.5^\circ$ products and to evaluate the errors of these products based on independent estimates from surface data and from atmospheric models over the western tropical Pacific (ocean only). Their major finding is that the root-mean-square error (RMSE) inferred from the SSM/I measurements is larger than the one based on surface data. They also find that the Tropical Rainfall

Measuring Mission (TRMM) microwave radiometer-based estimates perform better in the comparisons. Other multisensor studies like Dinku and Anagnostou (2006) remove the bias in the SSM/I-based precipitation estimates by calibrating the SSM/I estimate using a more accurate measurement, in this case TRMM precipitation radar (PR). They also show that the calibrated estimations have considerably less error. Others like Yin et al. (2008) include geographic location and topographic variables (such as surface roughness, slopes facing toward or away from moisture pathways, etc.) to improve the precipitation estimates from SSM/I measurements. Ferraro and Li (2002) use gauge measurements from the Oklahoma Mesonet network to estimate the errors in instantaneous SSM/I precipitation estimates over land. By incorporating an error model for Mesonet (as the truth measurement in their study), they estimate that the SSM/I-based precipitation rate over 0.5° , 1.0° , and 2.5° boxes has an error of 150%, 100%, and 70% respectively. This shows the high correlation between the resolution of data and the associated errors in the estimates. Similar results are also evident in the earlier study by Li et al. (1998).

Of the previous studies on PMW-based precipitation retrieval errors, perhaps the most relevant are those by McCollum et al. (2002) and Wolff and Fisher (2009). McCollum et al. (2002) make an evaluation of the bias in SSM/I-based precipitation retrievals over the contiguous United States (CONUS) by creating a bias-adjusted, ground-based radar estimate as the truth. They consider 3 years of data from SSM/I on board the *DMSP-F13*, *DMSP-F14*, and *DMSP-F15* satellites. The results show a dependency of the satellite-based data product errors on geographic location and climate. They find that retrievals based on SSM/I on board *F14* and *F15* overestimate precipitation over the central part of the United States by about 45%. However, they have used the Next Generation Weather Radar (NEXRAD) stage-III product, which is not a gauge-corrected product, and as a result, they had to implement a bias adjustment.

Wolff and Fisher (2009) used 4 years of data from SSM/I on board *DMSP-F13*, *DMSP-F14*, and *DMSP-F15*, as well as Advanced Microwave Sounding unit B (AMSU-B; on board *N15*, *N16*, and *N17*), Advanced Microwave Scanning Radiometer for Earth Observing System (AMSR-E on board the *Aqua* satellite), and TRMM Microwave Imager (TMI) and evaluated them with ground-based measurements from TRMM ground validation sites. Statistics such as probability density function (PDF), correlation coefficient, and performance skill score are reported. In general, they conclude that the PMW-based precipitation estimates tend to overestimate precipitation over land and ocean, and

TABLE 1. Merged satellite estimations of rainfall that use the SSM/I precipitation product based on the Ferraro and Marks (1995) algorithm.

Product name	Sources	Dates	Temporal resolution	Pixel size
Climate Prediction Center (CPC) morphing technique (CMORPH; Joyce et al. 2004, 2010)	PMW and IR	2002–present	0.5 h	0.25°
Precipitation Estimation from Remotely Sensed Imagery Using Artificial Neural Networks (PERSIANN; Hong et al. 2004; Hsu and Sorooshian 2008)	PMW and IR	2000–present	3 h	0.25°
CPC Merged Analysis of Precipitation (CMAP; Xie and Arkin 1997)	PMW and IR	1979–present	Monthly	2.5°
Global Precipitation Climatology Project (GPCP; Adler et al. 2003)	PMW and IR	1979–present	Monthly	2.5°

SSM/I and AMSU-B had lower performance skills compared to AMSR-E and TMI.

In a recent study, Vila et al. (2013) applied a new quality-control (QC) scheme to the antenna temperatures of SSM/I and SSMIS and evaluated monthly hydrological products such as rain rate, liquid water path, and total precipitable water. They used the Ferraro and Marks (1995) algorithm for rain-rate retrieval and concluded that the QC antenna temperatures produce a more accurate product on the monthly scale compared to the non-QC version. They also used a histogram matching technique to modify SSMIS temperatures and match them with the SSM/I reference across all seven channels. The results showed good agreement between the two sensors' products for all the analyzed variables.

In this study, we will use longer years of data products based on SSM/I instrument measurements to assess the errors in estimation of precipitation intensity over land. We also explore a larger spatial domain and introduce a new multiscale metric for evaluating rainfall products. In contrast to McCollum et al. (2002), we will use the NEXRAD stage-IV (NEXRAD-IV) radar product, which is a gauge-corrected rain-rate product, and we also use up to 6 years of data for our analysis. The statistics that are presented show the seasonality and intensity dependence of the errors in more detail. Moreover, we take advantage of their results showing the poor quality of radar products over mountainous regions and exclude those areas from our analysis.

This study specifically aims to quantify the retrieval errors in the precipitation product based on the suite of SSM/I instruments using the Ferraro and Marks (1995) algorithm. For ground validation, we use ground-based radar precipitation estimates. Specifically, we use the NEXRAD-IV product that is a merged reanalysis with gauge precipitation station observations. The NEXRAD-IV product provides realistic precipitation estimates that are less prone to error than radar-only estimates (Lin and Mitchell 2005). To have a more comprehensive evaluation, the error statistics of the SSM/I-based precipitation

products using instruments on board *DMSP-F13*, *DMSP-F14*, and *DMSP-F15* (hereafter referred to as SSM/I-13, SSM/I-14, and SSM/I-15, respectively) are presented. To distinguish between detection error and retrieval error, we have incorporated snow and freeze/thaw (FT) state measurements into our comparisons. The samples have been monitored for snow and FT status, and those with high snow percentage on the ground and/or frozen conditions have been removed from the analysis. The details of this monitoring are provided in section 2c.

Results show the significant and similar seasonal patterns in errors. The SSM/I-15 statistics reveal the effect of the interference from the radar calibration suite (RADCAL) that was activated on *DMSP-F15* on 14 August 2006. Our study area is over part of the CONUS where stage-IV data are available, and hence the focus is on land. Since many of the meteorological and hydrological hazard applications of Global Precipitation Measurement (GPM) data products with frequent refresh rates are over land, understanding the error structure and where the algorithms need improvement is important.

Section 2 of this paper presents the datasets used and the study region, along with the monitoring approach for removing detection errors. Section 3 includes the statistical measures and the results, while section 4 presents a discussion and conclusions.

2. Datasets and monitoring

a. Study area

The study region is a large portion of the CONUS contained within the region bounded by 31°37'30" and 47°37'30"N latitudes and 104°37'30" and 80°37'30"W longitudes. We have selected the region based on the results from McCollum et al. (2002) to exclude mountainous regions in which radar measurements are prone to errors. The spatial scale of comparisons is 0.25° (i.e., 0°15'00") for both NEXRAD- and SSM/I-based precipitation products. The NEXRAD data are coarse

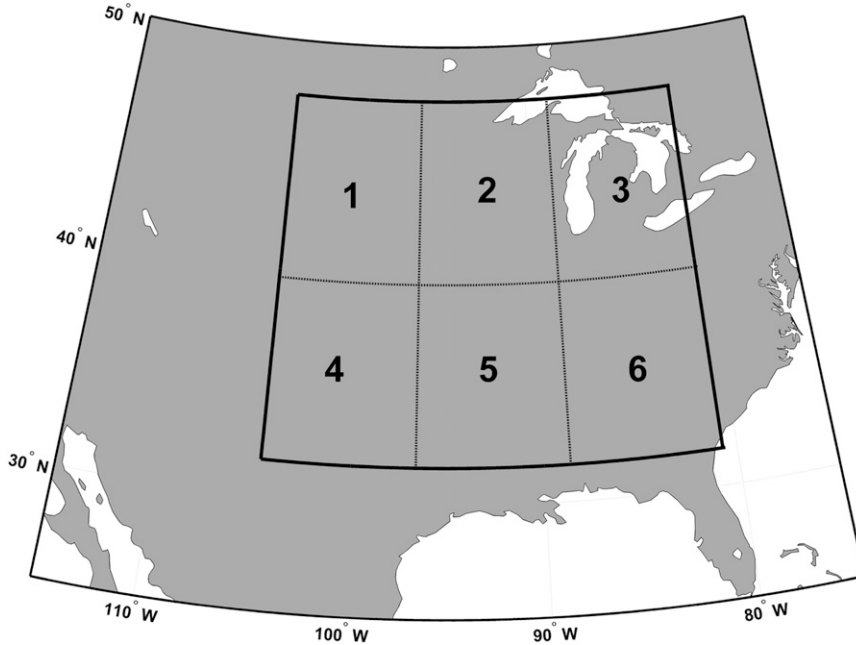


FIG. 2. The study area shown by the bold rectangular over the CONUS. The dashed lines show the six subregions defined for sampling.

grained to this resolution since their true resolution is considerably higher. The SSM/I-based products are posted at 0.25° even though the instrument measurement inputs are at similar or coarser resolutions. The match between the two products is not complete because of the swath limitations of the satellite instrument measurements. Missing pixel information also contributes to the mismatch. We therefore divide the region into six subregions, each of which covers $8^\circ \times 8^\circ$. Figure 2 shows the study area and the six subregions. We also exclude the pixels that fall over part of the Great Lakes in the northeastern part of the region and over the ocean in the southeastern part of the region because the Ferraro and Marks (1995) algorithm is only for precipitation retrieval over land. Some pixels close to these regions are also removed to mitigate water body contamination.

b. Data

The precipitation estimates based on SSM/I measurements are available through the Microwave Surface and Precipitation Products System (MSPPS) Orbital Data from the National Oceanic and Atmospheric Association (NOAA). These data products are available on orbital grids, and we map them into a $0.25^\circ \times 0.25^\circ$ grid using a nearest neighbor sampling that does not affect the marginal distribution of precipitation intensities. Nearest neighbor sampling is a method that assigns the value of the nearest SSM/I orbital pixel to the center of each grid box. The time domain for each of the satellites

is different, as listed in Table 2. The retrieval algorithm of the MSPSS product is based on Ferraro (1997). This algorithm uses a scattering approach for rain-rate retrieval over land. The scattering index (SI) is defined based on the earlier works by Grody (1991). The SI over land is defined as

$$SI_L = (451.9 - 0.44TB_{19V} - 1.775TB_{22V} + 0.00575TB_{22V}^2) - TB_{85V}, \quad (1)$$

in which SI_L is the scattering index over land, TB is the brightness temperature (K), and the subscripts denote the frequency of the vertical polarization channel used. This algorithm has been calibrated with ground-based radar measurements of rainfall, and the following equation is used to retrieve rain rate:

$$RR = 0.00513SI_L^{1.9468}, \quad (2)$$

where RR is the rain rate (mm h^{-1}). A minimum threshold of 10 K is set for SI based on earlier studies in

TABLE 2. Time domain and number of samples for each of the satellite platforms.

Sensor	Start date	End date	No. of samples
SSM/I-13	Jul 2003	Nov 2009	1525
SSM/I-14	Jul 2003	Aug 2008	1358
SSM/I-15	Jul 2003	Dec 2010	2696

the literature that results in a 0.45 mm h^{-1} minimum for rain-rate retrieval. Moreover, as the RR increases exponentially with SI based on Eq. (2), a maximum rain rate of 35 mm h^{-1} is also set for this algorithm, and values higher than that are set to 35 mm h^{-1} . This algorithm is also known as the NOAA/National Environmental Satellite, Data, and Information Service (NESDIS) algorithm for SSM/I.

The ground validation measurements are from the NEXRAD dataset obtained from the National Weather Service's ground-based Weather Surveillance Radar-1988 Doppler (WSR-88D) network (Fulton et al. 1998). The merged radar and gauge estimates produced by the 12 River Forecast Centers (RFCs) in CONUS is mosaicked on a 4-km grid at the National Centers for Environmental Prediction (NCEP). The result is a national product (NEXRAD-IV) that is available through the National Center for Atmospheric Research (NCAR) Earth Observing Laboratory (EOL; Lin and Mitchell 2005). We coarse grained these measurements spatially to a $0.25^\circ \times 0.25^\circ$ grid to be consistent with the SSM/I-based products. The temporal resolution of the data is hourly. The NEXRAD-IV data are available from January 2002 to present and cover the study period for each of the satellites considered here.

For generating samples, we match coincident measurements of NEXRAD-IV with each of the satellite products separately over the six subregions defined earlier. This means a sample is generated if the satellite overpass completely covers one of the subregions without any missing pixels. This condition is necessary for the application of the metrics defined in section 3. The result is a different number of samples for each satellite product in Table 2. In section 3d, the comparisons are made over the whole study region using climatological indices, but in the rest of the paper the pairs of samples that are generated for the subregions are compared.

The FT measurements are obtained from the National Snow and Ice Data Center (NSIDC) as part of the Making Earth System Data Records for Use in Research Environments (MEaSUREs) Global Record of Daily Landscape Freeze/Thaw Status, version 2 (Kim et al. 2011, 2012). This product is a global daily record of FT status derived using microwave observations from SSM/I and Scanning Multichannel Microwave Radiometer (SMMR). The data are provided on a Climate Modeling Grid (CMG) at 25-km grids. We inferred the morning and afternoon FT status separately using this dataset and excluded any pixel that had a frozen status at the time of measurement.

Snow data are from the Moderate Resolution Imaging Spectroradiometer (MODIS) instrument on board the *Terra* satellite. This dataset contains daily snow cover

data in a 0.05° CMG (Hall et al. 2006). We coarse grained these data to a $0.25^\circ \times 0.25^\circ$ spatial grid to match other measurements in our study. These measurements are used as a monitoring tool to exclude pixels that have a high percentage of snow cover from our analysis.

c. Monitoring algorithm

To filter out the detection errors from the analysis, we used FT and snow measurements. The logic behind this monitoring is that frozen or snow-covered ground has a high brightness temperature, and thus the instrument might detect these pixels as rainy (Ferraro et al. 1998). Therefore, we filtered out all the pixels that have a frozen condition at the time of measurement. As mentioned in the previous section, the FT data provide the morning and afternoon status separately. We used the morning status for any measurement taken before noon and the afternoon status for measurements taken after noon.

The snow cover data have been used in the sampling procedure that was described in section 2a. If more than 80% of the pixels in a sample are covered by snow (either partially or fully), the sample is rejected. On the other hand, the samples that are collected have a snow tag for each of their pixels. This tag is used during our analysis, and any pixel that is partially or fully covered by snow is not included in the calculations of metrics. For example, if we are calculating the probability of detection (POD), we assume that the pixel covered by snow does not exist.

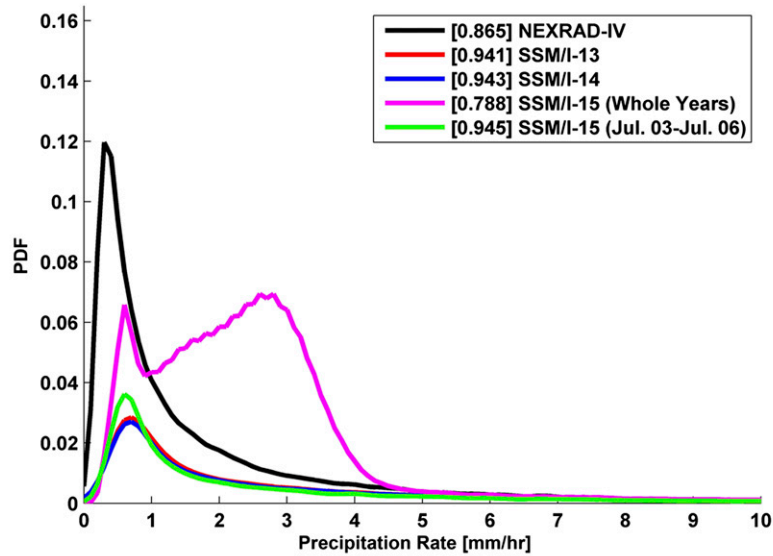
In section 3b, we present a comparison between two groups of samples: the first one only includes the samples with no snow cover and in thaw condition, and the second one contains only the samples with snow cover or frozen condition. This comparison shows that there is a considerable difference between the two groups, and it is necessary to remove the samples that have detection errors to have a better understanding of the retrieval errors.

3. Statistical comparisons

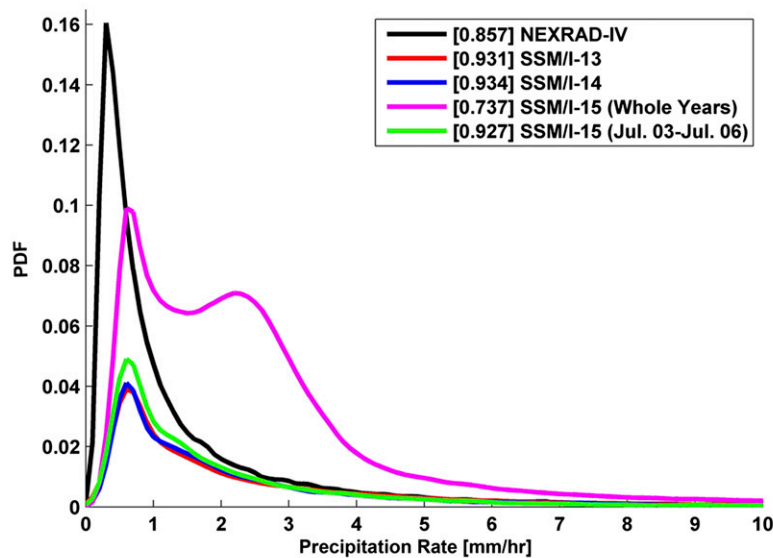
In this section, we consider several statistics to compare the SSM/I-based retrievals of precipitation with those based on NEXRAD-IV. These include the Jaccard distance at different rainfall thresholds, the POD, the false alarm ratio (FAR), and the PDF, as well as climatological indices of precipitation rate. Moreover, in section 3e we investigate the correspondence between precipitation-rate retrieval error and surface soil moisture. These are selected strategically in order to differentiate different types of errors.

a. Probability density function

Marginal PDFs give basic insight into systematic errors in the magnitude. Figure 3 shows the PDFs of



a) Probability Density Function of Precipitation Rate from Different Datasets (Summer)



b) Probability Density Function of Precipitation Rate from Different Datasets (Winter)

FIG. 3. PDF of rain rate from different data products. The numbers in brackets show the probability of no precipitation.

precipitation estimates from different datasets (SSM/I-13, SSM/I-14, SSM/I-15, and NEXRAD-IV) for both winter (October–March) and summer (April–September) months. The first result from these two comparisons is that the PDF of precipitation estimates from SSM/I-15 from all the years of data is very different than the other data products. However, if we remove the data after July 2006, the new PDF is more similar to the other two SSM/I-based PDFs, as well as the one from NEXRAD-IV. The reason for selecting this cutoff date is the activation of

the radar calibration suite on board *DMSP-F15* during August 2006 that has degraded the quality of measurements because of interference. This issue is investigated in more detail in the next section.

In general, the three SSM/I-based PDFs have the same shape and magnitude, but compared to the NEXRAD-IV PDF, they have a peak at a slightly higher precipitation rate, and the probabilities are in general lower. The reason is that the probability of no precipitation is higher for the SSM/I-based precipitation products

TABLE 3. Results of comparing Jaccard distance between non-snow-covered and thaw samples (group 1) with snow-covered and frozen samples (group 2).

Sensor	No. of samples		Mean and std dev of Jaccard	
	Group 1	Group 2	Group 1	Group 2
SSM/I-13	277	19	0.8217 ± 0.1713	0.9536 ± 0.0733
SSM/I-14	255	16	0.8414 ± 0.1555	0.9539 ± 0.0781
SSM/I-15	163	16	0.8441 ± 0.1639	0.9524 ± 0.0851

(bracketed numbers in Fig. 3). This can be partially due to the resolution differences in the coarse-resolution satellite data products and the high-resolution, ground-based radar product. Smaller precipitation events may be below the detection threshold of instruments with coarse resolution. Such resolution differences complicate merging PMW measurements into either gap-filling or calibrating other sensor measurements. Moreover, there is a slight difference between the peak of the PDF for SSM/I-13 and SSM/I-14 and the peak for SSM/I-15. Further analysis showed that sampling SSM/I-13 and SSM/I-14 for the same time period as SSM/I-15 does not change the qualitative differences between the PDFs. The different probability of no rain (shown in brackets in Fig. 3) might be a contributing factor that itself might be caused by the difference in the time of measurement between SSM/I-13 and SSM/I-14 compared to SSM/I-15 (see Fig. 7, described in greater detail below).

There is not a major difference between the PDFs from summer and winter months other than the probability of no precipitation. The slightly larger differences during the summer season are consistent with the resolution difference interpretation described in the previous paragraph. However, this does not necessarily confirm a causation. Note that the NEXRAD-IV measurements used to derive the PDF in Fig. 3 are concurrent with SSM/I-14 measurements. Results not shown here indicate that there are no noticeable differences between the PDF of precipitation from NEXRAD-IV if it is matched with data based on SSM/I-13 or SSM/I-15.

The PDF-based comparisons provide insights into the general distribution of magnitude errors. Because they are marginal distributions, they cannot characterize phase (location) errors, nor can the metric provide concise insights into the dependence on intensity. Other evaluation metrics that are capable of characterizing the latter attributes are POD and FAR. These two metrics are traditionally used and each is sensitive to a different type of error (but not the other). In the next section, we introduce a new metric that is related to both POD and FAR. This compact metric allows parsimonious evaluation of the data products.

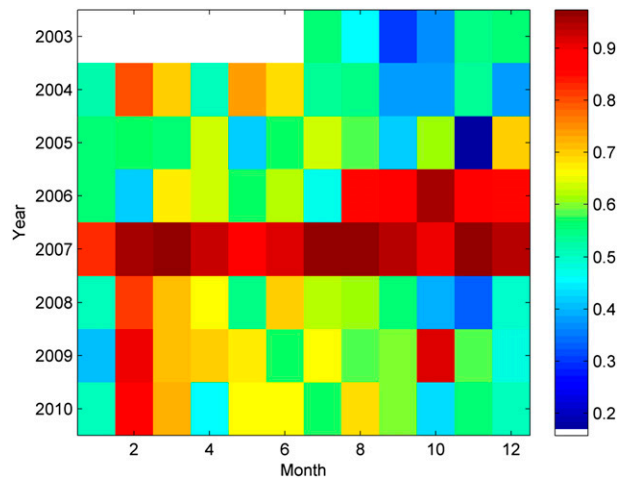


FIG. 4. Mean Jaccard distance between pairs of NEXRAD-IV and SSM/I-15 precipitation data products in each month at 3 mm h^{-1} threshold (white shows months with no data).

b. Jaccard distance

The metric used in this section to quantify proximity between two datasets is called the Jaccard distance. The Jaccard distance is used to evaluate dissimilarity of binary data (Tan et al. 2005). Let \mathbf{x} and \mathbf{y} be two objects that consists of n binary attributes. By comparing these two objects, four quantities can be defined:

$$\begin{aligned} f_{00} &= \text{number of attributes that } \mathbf{x} \text{ is 0 and } \mathbf{y} \text{ is 0;} \\ f_{10} &= \text{number of attributes that } \mathbf{x} \text{ is 1 and } \mathbf{y} \text{ is 0;} \\ f_{01} &= \text{number of attributes that } \mathbf{x} \text{ is 0 and } \mathbf{y} \text{ is 1;} \text{ and} \\ f_{11} &= \text{number of attributes that } \mathbf{x} \text{ is 1 and } \mathbf{y} \text{ is 1.} \end{aligned}$$

Based on the definitions of a 2×2 contingency table, f_{11} is the number of true positives (hits), f_{10} and f_{01} are the number of misses and false alarms, and f_{00} is the number of true negatives. Since Jaccard is a symmetric distance, there is no difference between f_{10} and f_{01} , and they can be used interchangeably. The Jaccard distance is defined as

$$J = 1 - \frac{f_{11}}{f_{01} + f_{10} + f_{11}}. \quad (3)$$

The Jaccard distance will have a value between zero and one; a smaller value of Jaccard distance shows that the two images are more similar.

The appendix relates the Jaccard distance to FAR and POD. Both the FAR and POD also depend on various combinations of f_{01} and f_{10} errors. But whereas neither POD nor FAR contain both f_{01} and f_{10} errors, neither is a complete measure of all error types in itself. The Jaccard distance conveniently combines the two error types and the information captured by POD and FAR

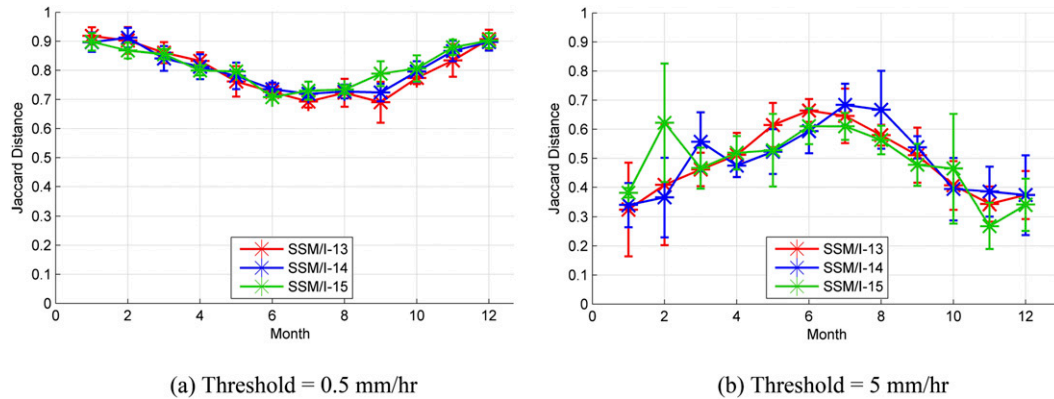


FIG. 5. Mean and one std dev of Jaccard distance between NEXRAD-IV and different satellite platform precipitation data products in each month.

into a single and parsimonious metric. The appendix contains the relationship between the metrics, and Fig. A1 in the appendix shows that the Jaccard distance is an equitable combination of both FAR and POD. The appendix also includes simple case examples where an error type is missed by either FAR or POD but has impacts on the magnitude of the Jaccard distance.

First, we provide the result of a comparison between two groups of samples, as mentioned in section 2c. These samples are only taken from region 1 in Fig. 2 and are only from the months of October and November. Group 1 has only samples that are free of snow and have a thaw condition at all times; group 2 has only samples that have snow cover on the ground or a frozen condition at the time of measurement. Table 3 presents the results for each of the three platforms along with the number of samples. This shows that there is a considerable difference between the means of the two groups, and group 2 has a higher mean. This proves the necessity for filtering out the snow-covered and frozen samples to provide a better analysis of the retrieval errors.

We apply the metric to compare coincident SSM/I and NEXRAD-IV precipitation intensity data products. To gain more concise insight, we have evaluated the Jaccard distance at different thresholds of precipitation intensity (0, 0.5, 1.0, 1.5, 3.0, 5.0, 7.0, and 10.0 mm h⁻¹) in different seasons. Figure 4 shows the mean of the Jaccard distance in each month for a threshold of 3 mm h⁻¹ from SSM/I-15 measurements. The general pattern in this figure is also present for other thresholds, albeit at different magnitudes (see analysis and figures discussed below). Figure 4 shows that there is greater dissimilarity (larger Jaccard distance and closer to unity) for the period between August 2006 and December 2007. This is more distinguished at lower-magnitude thresholds. This shows the effect of RADCAL suite that was activated on *DMSP-F15* during August 2006 that produced interference with the

85-GHz channel on the unit. This issue is described in the technical report by the Remote Sensing Systems (RSS) group (Hilburn 2009). This pattern disappears after 2007, and the only reason that we can find for that is the drift in the orbit of the *DMSP-F15* in early 2008. It has been reported that the effect of the interference from the RADCAL suite is dependent on the thermal environment that changes with the drift of the satellite (Hilburn and Wentz 2008). However, based on the observations of Hilburn and Wentz (2008), the interferences exist with an intermittent pattern after 2007. Therefore, in the remainder of this paper, all the statistics that are presented for the SSM/I-15 dataset will exclude the measurements after August 2006 unless otherwise indicated. Comparing the results of Jaccard distance for the pairs of NEXRAD-IV and SSM/I-13 and SSM/I-14, no systematic anomalous patterns can be detected.

More detailed examination of the Jaccard distance between the NEXRAD-IV and SSM/I estimates reveals that in low thresholds during the summer, the SSM/I-based precipitation estimates have better performance (low Jaccard values). During winter, the SSM/I land precipitation retrieval algorithm appears to have larger errors. This pattern is reversed at higher thresholds. Figure 5 shows the monthly mean of Jaccard distance at two different thresholds for all the three instruments. There are clearly large differences between Figs. 5a and 5b. The seasonality error magnitudes are convex up and down, depending on the precipitation-rate threshold.

Figure 6 also illustrates the mean and one standard deviation of Jaccard distance over all the samples at different thresholds. There is a decreasing trend of the Jaccard distance with respect to the threshold. The retrieval algorithms have greater challenges with low precipitation rates than higher precipitation rates. As was mentioned in section 2b, the Ferraro and Marks (1995) algorithm has a 0.45 mm h⁻¹ minimum limit that

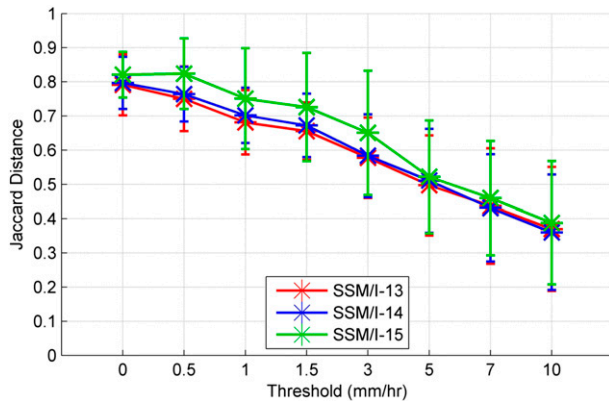


FIG. 6. Mean and one std dev of Jaccard distance between NEXRAD-IV and different satellite platform precipitation data products at different thresholds.

is also contributing to this problem. Depending on the application, this difference in errors may be compensated by the application itself (e.g., flood forecasts).

The last evaluation using Jaccard distance is presented to show the effect of diurnal cycle on the quality of measurements. Figure 7 shows the box plot of Jaccard distance at threshold 0 mm h^{-1} for each of the sensors as a function of time of the day (local time). These plots are derived using samples that are only from regions 2 and 5 in Fig. 2, as they have a more similar longitude compared to the whole study region. This figure shows that there is not a general pattern for quality of the measurements with respect to the time of the measurement. It should be noted that the reason for the box plot of SSM/I-14 to be spread over several hours compared to SSM/I-13 is the drift of the satellite during the years 2003–08. This is evident to some extent in the SSM/I-15 plot as well. Evaluation of the Jaccard distance at higher thresholds revealed similar trends for all the platforms.

c. POD and FAR

The Jaccard distance is a metric of proximity in two binary fields. It is related to both POD and FAR, which each capture a separate and distinct type of error. Some applications may be sensitive to one but not the other. For the sake of completeness, we also report on the dependencies of errors captured by POD and FAR as a function of season.

The POD metric shows the quality of capturing precipitation in the estimates. The FAR captures possible overestimation of precipitating areas. Ebert (2007) provides a comprehensive review of the statistics. Here, we use POD and FAR to evaluate the SSM/I precipitation product with respect to NEXRAD-IV product.

Figure 8 shows the mean and one standard deviation of POD and FAR for all the three platforms across

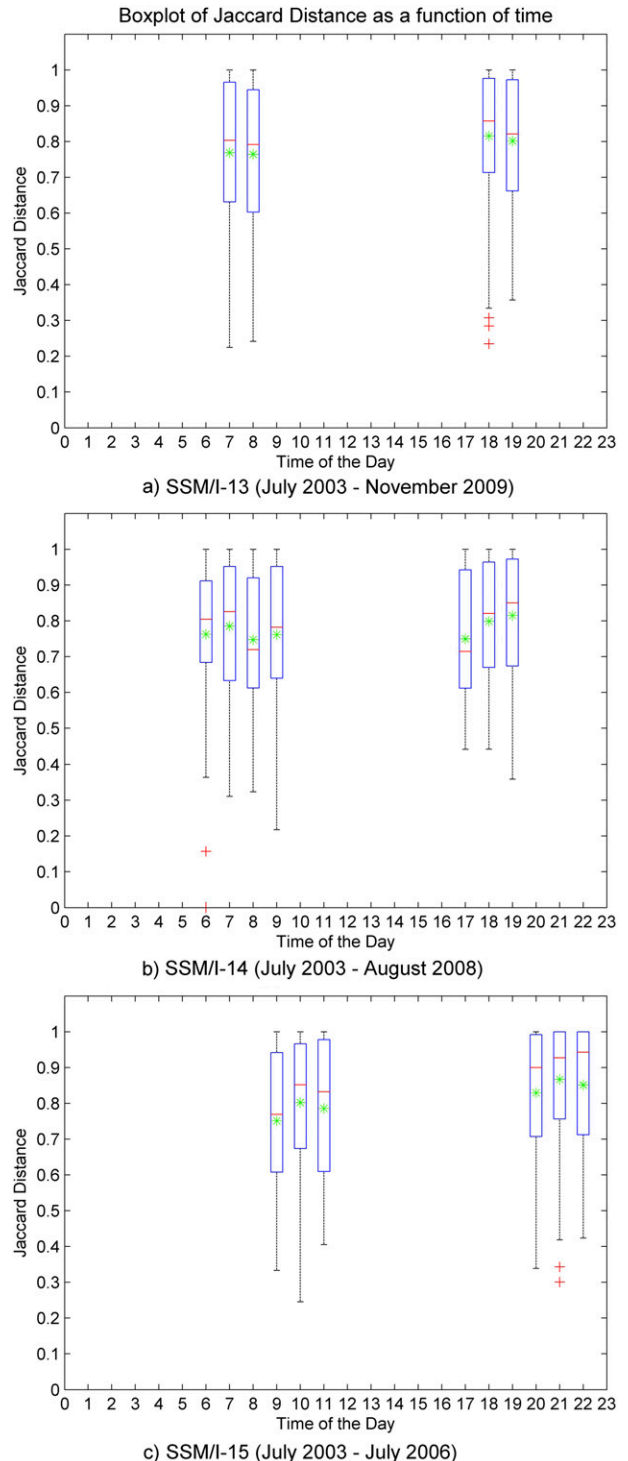


FIG. 7. Box plot of Jaccard distance as a function of the time of day (local time) for (a) SSM/I-13, (b) SSM/I-14, and (c) SSM/I-15. The central red line indicates the median, the edges of the box are 25th and 75th percentiles, the whiskers show the most extreme values, and outliers are plotted as red crosses. The mean is also plotted as a green asterisk.

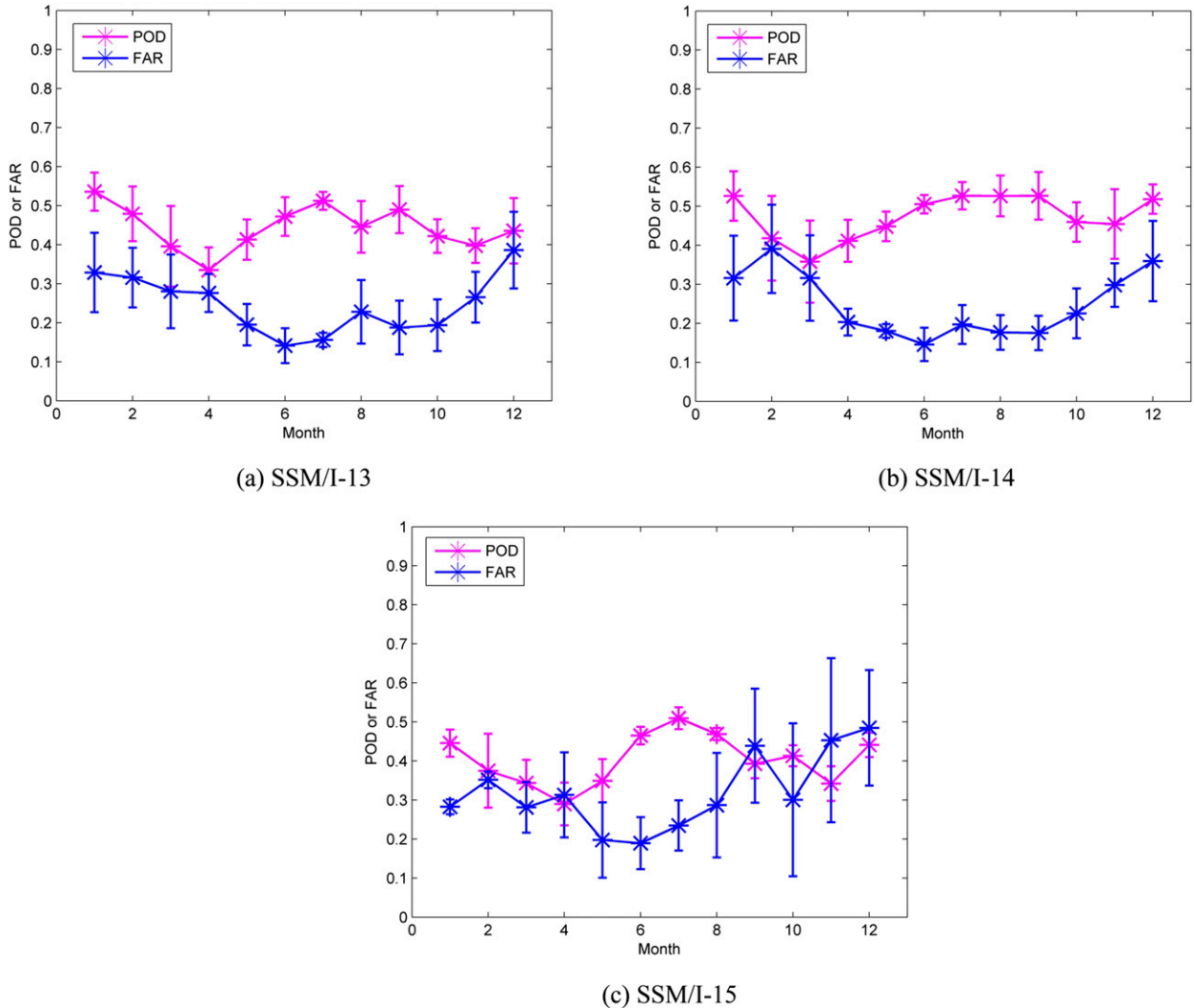


FIG. 8. Mean and one std dev of POD and FAR for SSM/I precipitation data products over different months.

different months. For SSM/I-15, we have only included data from July 2003 until July 2006. The general trend for all the platforms is that during summer months POD increases and FAR decreases, that is, better estimates are obtained during summertime. This pattern is consistent with the Jaccard distance at lower thresholds; however, at higher thresholds the Jaccard distance had a different pattern that provided another perspective. The pattern revealed by Jaccard distance at different thresholds (Fig. 5) indicates that moderate to high precipitation rates are estimated more accurately in this algorithm. The fact that this algorithm does not have a classification scheme to distinguish between different precipitation regimes (e.g., stratiform versus convective) can be a contributing factor to the different performance patterns at different thresholds.

d. Geographical distribution of errors

Whereas PDF, Jaccard distance, POD, and FAR metrics allow stratification of errors by season, intensity magnitude, and instrument, they do not allow investigation of possible systematic geographical errors that may be associated with topography, climate regime, and other site-specific contributions to errors in retrieval. In this section, the results of climatological comparison of SSM/I and NEXRAD-IV are presented by mapping mean values. For this comparison, concurrent precipitation estimates based on SSM/I and NEXRAD-IV measurements over the study region are averaged, and the mean of the precipitation rates are presented in Fig. 9. We have only selected the concurrent measurements for each platform; therefore, the two climatological averages are statistically comparable.

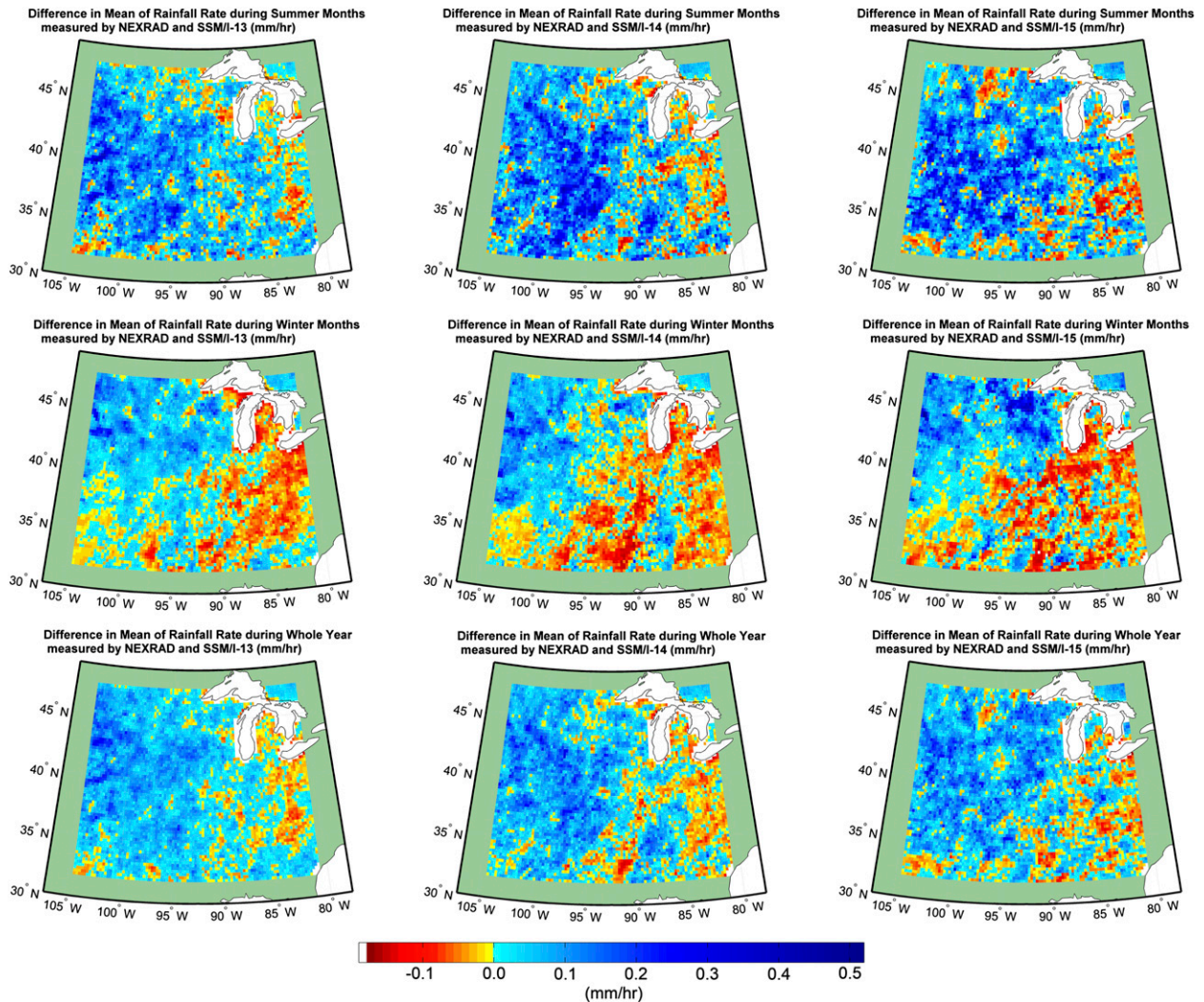


FIG. 9. Difference in mean of SSM/I and NEXRAD-IV precipitation data products for (left) SSM/I-13, (middle) SSM/I-14, and (right) SSM/I-15 over (top) summer months (April–September, inclusive), (middle) winter months (October–March, inclusive), and (bottom) the whole year.

Rows in Fig. 9 from top to bottom correspond to summer differences, winter differences, and whole-year differences in the SSM/I instrument-based precipitation products and NEXRAD-IV. Summer is defined as April–September (inclusive) and winter is defined as October–March (inclusive). For SSM/I-15, only the period not affected by RADCAL is used (from July 2003 to July 2006).

A useful backdrop for interpreting the difference maps is the precipitation climatology itself, which is sampled according to the availability of satellite-based estimates. Figure 10 shows the precipitation climatology evident in the NEXRAD-IV data product. In deriving this climatology, we have sampled NEXRAD-IV at the times when SSM/I-14 swath and overpass coverage is available. This conditional sampling has small and almost imperceptible effects on the true climatology when

all NEXRAD-IV data are used (not shown). Furthermore, the choice of instrument other than SSM/I-14 does not change the conclusions. The issues are more closely tied with the algorithms themselves.

Figure 10 shows a strong a gradient of mean precipitation over the region from northwest to southeast. Superimposed on the difference maps in Fig. 9, a systematic error with geographical structure becomes evident. There are three major differences between the NEXRAD-IV estimates and the SSM/I precipitation data products:

- SSM/I-based precipitation products mostly overestimate the precipitation rate; therefore, the difference in their mean statistic is mostly positive. There are regions where SSM/I underestimates the precipitation

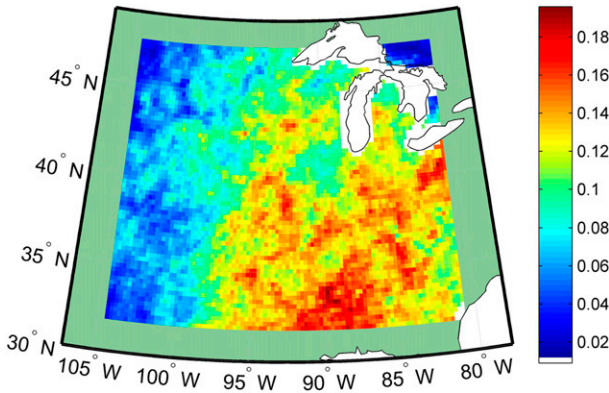


FIG. 10. Mean precipitation rate based on NEXRAD-IV sampled concurrent to SSM/I measurements over the region.

rate climatologically, but their area is limited in extent when compared to those that are overestimated.

- All three platforms and their instrument and data products have similar spatial patterns for summer, winter, and the whole year. For example, during summer SSM/I-13, SSM/I-14 and SSM/I-15 show similar differences in mean precipitation over the study region. During winter, all three SSM/I products overestimate over the western and northwestern parts of the study region. This is a dominant feature in all three, and it affects the whole-year difference plots. The dominant differences are localized in the western and northwestern part of the region.
- In the southeastern part of the region, all the three platforms have small negative difference values. This region has the highest precipitation rates climatologically. The SSM/I-based precipitation estimates have better quality over the southeastern part of the study region that generally has higher precipitation-rate magnitudes. This is consistent with the findings from Jaccard distance at different thresholds (Fig. 5) that this algorithm has better performance on moderate to high precipitation rates.

These conclusions are consistent with those evident in the PDFs (Fig. 3).

e. Error dependence on surface soil moisture

One of the factors affecting the quality of precipitation retrieval from microwave measurements is variable land surface emissivity that is partially due to dynamic surface soil moisture (Ferraro et al. 2013). In situ or satellite estimates of surface soil moisture are limited by their spatial and/or temporal coverage. Therefore, we used the Antecedent Precipitation Index (API) as an index of soil moisture content to investigate correspondence between the precipitation estimation error and estimated soil moisture. API is defined as

$$\text{API}_t = K(\text{API}_{t-1}) + P_t, \quad (4)$$

where API_t is the API on day t , API_{t-1} is the API on the preceding day $t - 1$, P_t is the precipitation on day t , and K is a constant decay factor. The variable K is dimensionless, and the other three parameters in this equation have units of length (in this case, millimeters). The value of K controls the decay or loss rate of surface soil moisture. Based on literature values of the application of this filter to precipitation in order to produce estimates of surface soil moisture, we use a typical value of 0.93 for K . Daily APIs are estimated using the 24-h accumulations of NEXRAD measurements.

For each measurement pixel, we calculate the error of the SSM/I estimation with respect to NEXRAD. We segment the errors conditional on values of API over that pixel from the day before. The API of the day of observation is affected by the current storm; however, the API from the day before only indicates the soil moisture content as a result of preceding storms and at the time of measurement. Use of same-day API did not appreciably change the conclusions. To enhance the sample size, we have combined the measurement errors from SSM/I-13, SSM/I-14, and SSM/I-15.

Figure 11 shows box plots of errors in SSM/I precipitation estimation versus API values. This figure includes six plots, one for each of the subregions. In each subregion, the number of data for each box are equal, and the number of data for each subregion are as follows: subregion 1, 23 635; subregion 2, 27 355; subregion 3, 16 653; subregion 4, 12 856; subregion 5, 23 632; and subregion 6, 30 457. Similar to the other box plot in Fig. 7, the edges of the boxes are the 25th and 75th percentiles, and the central red line indicates the median. The mean is also plotted as a green asterisk. No consistent trend is detected in subregions 1–4; however, in subregions 5 and 6, the mean and median of the error decrease with increases in API. The results of a statistical hypothesis test (t test) show that in 86% of the cases the mean of each of the error box plots is different than the others in the same subregion at the 5% significance level.

This analysis shows that the errors in SSM/I precipitation estimations are dependent on dynamical changes of the surface conditions. Land surface emissivity changes that are partially driven by dynamics of surface soil moisture can affect the precipitation-rate retrieval performances. A possible future path is to use surface soil moisture retrievals from the Soil Moisture Active Passive (SMAP) mission to estimate the soil moisture contribution to changing surface emissivity (Ferraro et al. 2013).

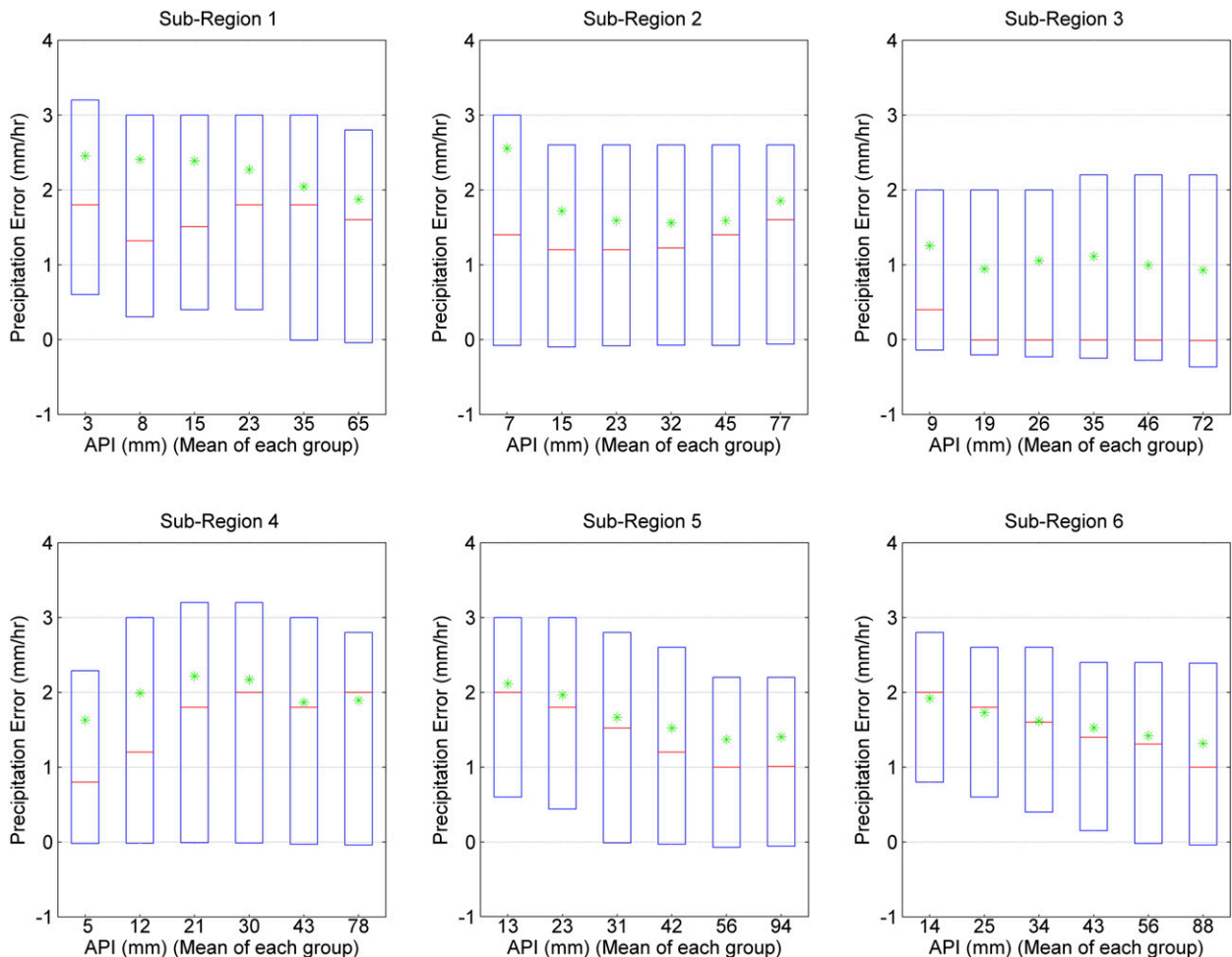


FIG. 11. Box plot of SSM/I-based precipitation-rate error as a function of API in each subregion. The central red line indicates the median, the edges of the box are 25th and 75th percentiles, and the mean is plotted as a green asterisk.

4. Summary

In this study, we investigate and diagnose the errors in the precipitation products based on the Special Sensor Microwave Imager (SSM/I) instrument on board the *DMSP-F13*, *DMSP-F14*, and *DMSP-F15* platforms. We use the gauge-corrected, ground-based radar product NEXRAD-IV to diagnose the dependencies of the errors on precipitation intensity, season, platform, and other factors. The stratification of the errors according to these attributes is made possible by using extended duration and large domain comparison datasets. Data products from three DMSP platforms and the extensive NEXRAD record are used. The stratification identifies priorities for ways of improving the passive-microwave-based precipitation retrieval algorithms over land. These algorithms are currently used to calibrate global precipitation products that use infrared brightness temperatures from

instruments on geostationary platforms as their major inputs.

We show that current SSM/I-based precipitation products are positively biased in magnitude. The bias is less at higher intensities and in geographic locations where precipitation rates are generally higher. Several marginal distribution and magnitude and phase error statistics are also used in this study to evaluate SSM/I-based precipitation products. The Jaccard distance is introduced as a compact and concise metric to evaluate precipitation products. It is shown that the metric captures errors that have distinct seasonal and magnitude-dependent characteristics. Together with its constituent POD and FAR metrics, we show that the SSM/I-based precipitation products generally overestimate precipitating areas during the winter months by estimating low-magnitude precipitation rates outside of the precipitation clusters. This contributes to the noticeable dependence of the Jaccard distance metric on intensity magnitude. The SSM/I-based

products provide better estimates during summertime when compared to the winter season.

Month by month comparisons of the metric across platforms and instruments reveal a major anomaly starting in August 2006 and ending in December 2007. During this period, the products based on SSM/I-15 are worse compared to the rest of the study period. This is consistent with the timing of the activation of the radar calibration (RADCAL) suite on board *F15* that interferes with the 85-GHz channel.

The effects of dynamic surface soil moisture on the quality of precipitation retrieval shows a strong connection between the estimation error and changing soil moisture. More accurate land surface emissivity estimates can possibly improve precipitation-rate retrievals over land. The future SMAP mission provides accurate fine-spatial-scale measurements of soil moisture that can be combined with precipitation retrieval algorithms to improve the accuracy of precipitation estimations.

There are inherent challenges associated with retrieval of precipitation over land based on the measurements in the set of channels afforded by SSM/I and its heritage instruments. The sources of emissions and scattering cannot all be characterized by the finite measurements. Simple distributional corrections such as probability matching work well on the training datasets, but they may not generally extend to times and regions where both ground validation and retrievals are not used in the matching. We suggest that the paradigm for generating and using data products needs to be revisited in the case of such a challenging and important retrieval problem. The error patterns in SSM/I-based precipitation products are not structured in simple ways, and they cannot be easily modeled and removed. Perhaps we should go beyond deterministic product generation and incorporate uncertainty in the description of the products. There is an emerging trend toward stochastic and ensemble-based approaches to merging and interpreting data products. If we generate a population of equally probable prior replicates based on the SSM/I measurements and update the prior probabilities using the historical error likelihood, then it is possible to generate a posterior population of precipitation replicates that are ranked based on the probability of being a characterization of the true situation. Each of these replicates will be consistent with the original measurement while having some added noise. This study aimed at characterizing the types and dependency attributes of retrieval errors that is a necessary first step toward this goal.

Acknowledgments. The authors thank the anonymous reviewers for their helpful comments and suggestions to enhance the quality of the paper. This study is partially

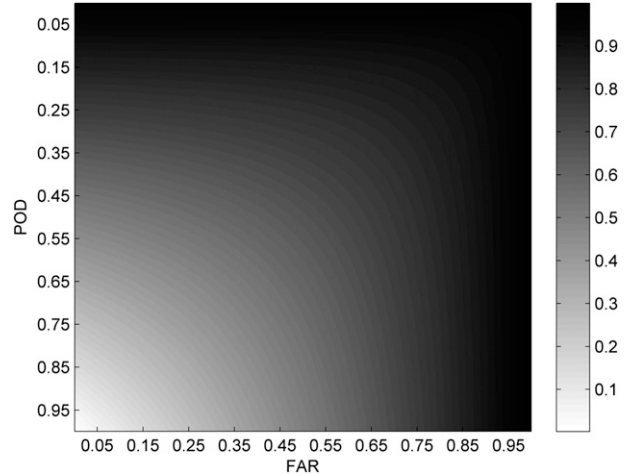


FIG. A1. Jaccard distance for different combinations of POD and FAR.

supported by a joint grant to the Massachusetts Institute of Technology and the Masdar Institute for Science and Technology.

APPENDIX

Comparing Jaccard Distance with POD and FAR

a. Definitions

Assume two measurements—one is the true measurement (called T hereafter) and the other is a second measurement to be validated versus the true one (called V hereafter). Based on the definitions provided in [section 3](#), the Jaccard distance, POD and FAR are

$$J = 1 - \frac{f_{11}}{f_{10} + f_{01} + f_{11}} = \frac{f_{10} + f_{01}}{f_{10} + f_{01} + f_{11}}, \quad (\text{A1})$$

$$\text{POD} = \frac{f_{11}}{f_{11} + f_{10}}, \quad \text{and} \quad (\text{A2})$$

$$\text{FAR} = \frac{f_{01}}{f_{11} + f_{01}}. \quad (\text{A3})$$

The main difference between J and POD is that J considers both the hits and misses in the measurements while POD only captures hits. On the other hand, FAR only deals with misses. Therefore, the combined outcome of the POD and FAR can be inferred from J itself. However, depending on application, it might be advantageous to distinguish between POD and FAR.

It is possible to relate the Jaccard distance uniquely to POD and FAR. Based on Eq. (A2),

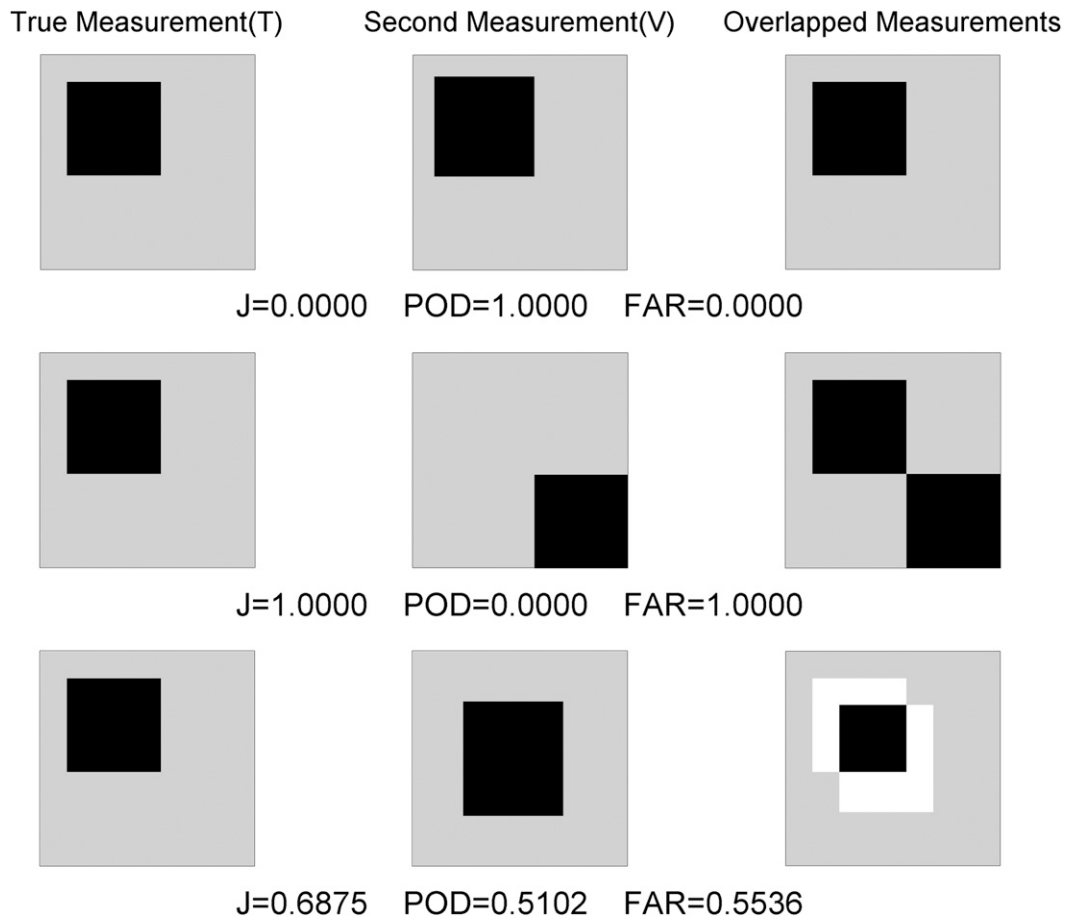


FIG. A2. Example 1 comparing J , POD, and FAR (black represents a feature in T or V and an overlapping feature in the overlapped measurement, white represents a nonoverlapping feature in the overlapped measurement, and gray represents no feature).

$$f_{10} = \frac{(1 - \text{POD})f_{11}}{\text{POD}}. \quad (\text{A4})$$

Using Eq. (A3),

$$f_{01} = \frac{(\text{FAR})f_{11}}{1 - \text{FAR}}. \quad (\text{A5})$$

Substituting Eqs. (A4) and (A5) into Eq. (A1) results in

$$J = \frac{\frac{(1 - \text{POD})f_{11}}{\text{POD}} + \frac{(\text{FAR})f_{11}}{1 - \text{FAR}}}{\frac{(1 - \text{POD})f_{11}}{\text{POD}} + \frac{(\text{FAR})f_{11}}{1 - \text{FAR}} + f_{11}}. \quad (\text{A6})$$

The f_{11} terms can be eliminated to write J only in terms of POD and FAR:

$$J = \frac{(\text{FAR})(\text{POD}) + (1 - \text{POD})(1 - \text{FAR})}{(\text{FAR})(\text{POD}) + (1 - \text{POD})(1 - \text{FAR}) + (\text{POD})(1 - \text{FAR})}. \quad (\text{A7})$$

Figure A1 shows the Jaccard distance as a function of POD and FAR. The Jaccard distance changes with different combinations of POD and FAR. The Jaccard distance captures both types of errors measured by POD and FAR.

b. Examples

In this section, we provide a series of synthetic examples to compare J , POD, and FAR. In all cases, the true measurement is the same. Figure A2 shows three examples: the first column shows the true measurement

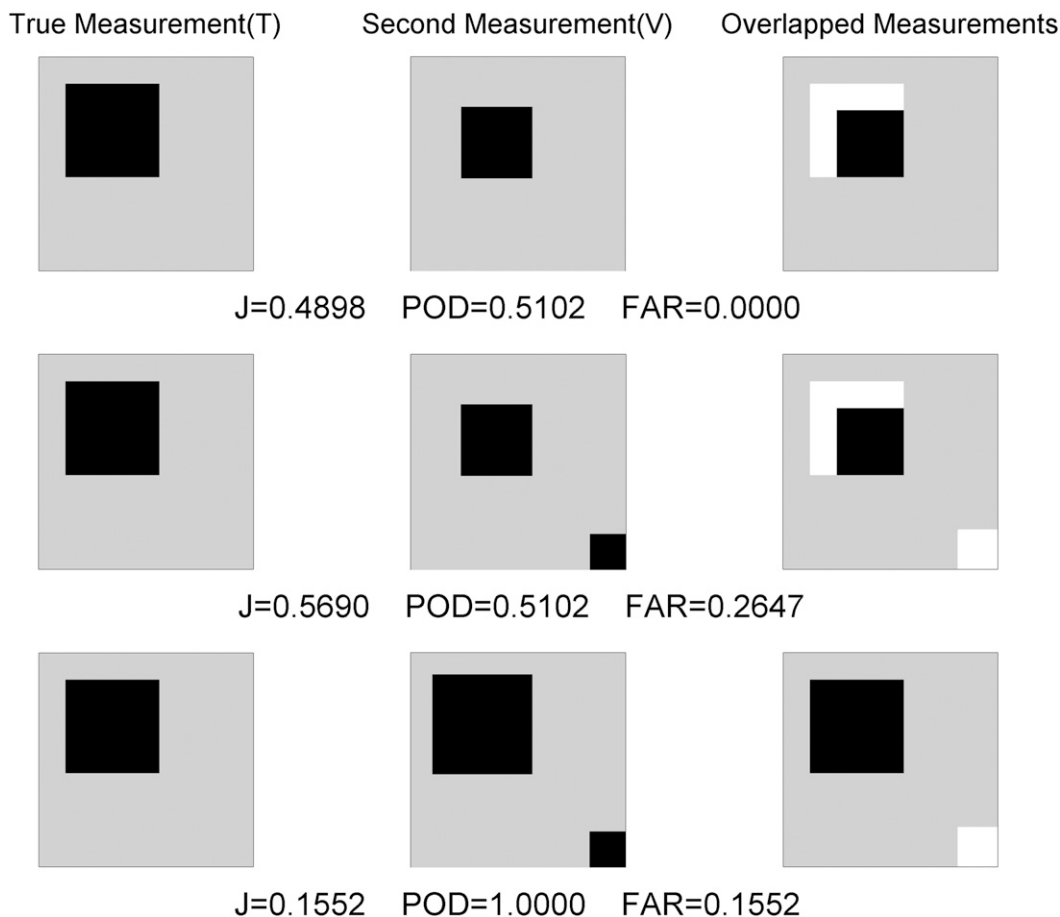


FIG. A3. Example 2 comparing J , POD, and FAR (black represents a feature in T or V and an overlapping feature in the overlapped measurement, white represents a nonoverlapping feature in the overlapped measurement, and gray represents no feature).

(i.e., T), the second column shows the second measurement (i.e., V) to be compared, and the last column shows the overlapped measurements. In the first row, T and V are the same, so $J = FAR = 0$ and $POD = 1$. For the second row, V is shifted so as not to overlap with T . This is the case with the most difference between T and V , so $J = FAR = 1$ and $POD = 0$. The third row shows a situation in between: both T and V are overlapping in some pixels, but not all of them. As a result, POD, FAR, and J are all intermediate between 0 and 1.

Figure A3 shows another set of examples with the same T . Here, the first row has a V that has a smaller true area with respect to T , so there is no false detection, that is, $FAR = 0$. However, POD and J are not equal to 1, as the two images are different. If we add some false area to V (as in the second row), the POD does not change, but J and FAR change. This shows that POD is not sensitive to false detected areas. So, if there is a V that is just

overestimating the true area, it will have a $POD = 1$, although the V and T will not be the same. At the same time, J changes between rows 1 and 2. Thus, J is sensitive to both hits and false detections. Row 3 shows how POD, FAR, and J change when there is spatial overestimation.

In some special cases FAR will have the exact value as J . For example, if $f_{10} = 0$, then $J = FAR$. This happens when there are no misses in the detection.

REFERENCES

- Adler, R. F., and Coauthors, 2003: The version-2 Global Precipitation Climatology Project (GPCP) monthly precipitation analysis (1979–present). *J. Hydrometeor.*, **4**, 1147–1167, doi:10.1175/1525-7541(2003)004<1147:TVGPCP>2.0.CO;2.
- Bell, T. L., P. K. Kundu, and C. D. Kummerow, 2001: Sampling errors of SSM/I and TRMM rainfall averages: Comparison with error estimates from surface data and a simple model. *J. Appl. Meteor.*, **40**, 938–954, doi:10.1175/1520-0450(2001)040<0938:SEOSIA>2.0.CO;2.

- Berg, W., C. Kummerow, M. Sapiano, N. Rodrigues-Alvarez, and F. Weng, 2012: A fundamental climate data record of microwave brightness temperature data from 25 years of SSM/I and SSMIS observations. *GEWEX News*, No. 22, International GEWEX Project Office, Silver Spring, MD, 4–5.
- Dinku, T., and E. N. Anagnostou, 2006: TRMM calibration of SSM/I algorithm for overland rainfall estimation. *J. Appl. Meteor. Climatol.*, **45**, 875–886, doi:10.1175/JAM2379.1.
- Ebert, E. E., 2007: Methods for verifying satellite precipitation estimates. *Measuring Precipitation from Space*, V. Levizzani, P. Bauer, and F. J. Turk, Eds., Springer, 345–356.
- Ferraro, R. R., 1997: Special sensor microwave imager derived global rainfall estimates for climatological applications. *J. Geophys. Res.*, **102**, 16 715–16 735, doi:10.1029/97JD01210.
- , and G. F. Marks, 1995: The development of SSM/I rain-rate retrieval algorithms using ground-based radar measurements. *J. Atmos. Oceanic Technol.*, **12**, 755–770, doi:10.1175/1520-0426(1995)012<0755:TDSORR>2.0.CO;2.
- , and Q. Li, 2002: Detailed analysis of the error associated with the rainfall retrieved by the NOAA/NESDIS Special Sensor Microwave/Imager algorithm 2. Rainfall over land. *J. Geophys. Res.*, **107**, 4680, doi:10.1029/2001JD001172.
- , E. A. Smith, W. Berg, and G. J. Huffman, 1998: A screening methodology for passive microwave precipitation retrieval algorithms. *J. Atmos. Sci.*, **55**, 1583–1600, doi:10.1175/1520-0469(1998)055<1583:ASMFPM>2.0.CO;2.
- , and Coauthors, 2013: An evaluation of microwave land surface emissivities over the continental United States to benefit GPM-era precipitation algorithms. *IEEE Trans. Geosci. Remote Sens.*, **51**, 378–398, doi:10.1109/TGRS.2012.2199121.
- Fulton, R. A., J. P. Breidenbach, D. J. Seo, and D. A. Miller, 1998: The WSR-88D rainfall algorithm. *Wet. Forecasting*, **13**, 377–395, doi:10.1175/1520-0434(1998)013<0377:TWRA>2.0.CO;2.
- Grody, N. C., 1991: Classification of snow cover and precipitation using the Special Sensor Microwave Imager. *J. Geophys. Res.*, **96**, 7423–7435, doi:10.1029/91JD00045.
- Hall, D. K., V. V. Salomonson, and G. A. Riggs, 2006: MODIS/Terra snow cover daily L3 global 0.05Deg CMG, version 5. National Snow and Ice Data Center, Boulder, CO, digital media. [Available online at <http://nsidc.org/data/mod10c1>.]
- Hilburn, K. A., 2009: Including temperature effects in the F15 RADCAL correction. Remote Sensing Systems Tech. Rep. 051209, 11 pp. [Available online at http://images.remss.com/papers/RSS_TR051209_RADCAL.pdf.]
- , and F. J. Wentz, 2008: Mitigating the impact of RADCAL beacon contamination on F15 SSM/I ocean retrievals. *Geophys. Res. Lett.*, **35**, L18806, doi:10.1029/2008GL034914.
- Hong, Y., K.-L. Hsu, S. Sorooshian, and X. Gao, 2004: Precipitation estimation from remotely sensed imagery using an artificial neural network cloud classification system. *J. Appl. Meteor.*, **43**, 1834–1853, doi:10.1175/JAM2173.1.
- Hsu, K., and S. Sorooshian, 2008: Satellite-based precipitation measurement using PERSIANN system. *Hydrological Modeling and the Water Cycle*, S. Sorooshian et al., Eds., Springer, 27–48.
- Huffman, G. J., and Coauthors, 2007: The TRMM multisatellite precipitation analysis (TMPA): Quasi-global, multiyear, combined-sensor precipitation estimates at fine scales. *J. Hydrometeorol.*, **8**, 38–55, doi:10.1175/JHM560.1.
- Joyce, R. J., J. E. Janowiak, P. A. Arkin, and P. Xie, 2004: CMORPH: A method that produces global precipitation estimates from passive microwave and infrared data at high spatial and temporal resolution. *J. Hydrometeorol.*, **5**, 487–503, doi:10.1175/1525-7541(2004)005<0487:CAMTPG>2.0.CO;2.
- , P. Xie, Y. Yarosh, J. E. Janowiak, and P. A. Arkin, 2010: CMORPH: A “morphing” approach for high resolution precipitation product generation. *Satellite Rainfall Applications for Surface Hydrology*, M. Gebremichael and F. Hossain, Eds., Springer, 23–37.
- Kidd, C., D. R. Kniveton, M. C. Todd, and T. J. Bellerby, 2003: Satellite rainfall estimation using combined passive microwave and infrared algorithms. *J. Hydrometeorol.*, **4**, 1088–1104, doi:10.1175/1525-7541(2003)004<1088:SREUCP>2.0.CO;2.
- Kim, Y., J. S. Kimball, K. C. McDonald, and J. Glassy, 2011: Developing a global data record of daily landscape freeze/thaw status using satellite passive microwave remote sensing. *IEEE Trans. Geosci. Remote Sens.*, **49**, 949–960, doi:10.1109/TGRS.2010.2070515.
- , —, J. Glassy, and K. C. McDonald, 2012: MEASURES global record of daily landscape freeze/thaw status, version 2. National Snow and Ice Data Center, Boulder, CO, doi:10.5067/MEASURES/CRYOSPHERE/nsidc-0477.002.
- Krishnamurti, T. N., and Coauthors, 2001: Real-time multianalysis-multimodel superensemble forecasts of precipitation using TRMM and SSM/I products. *Mon. Wea. Rev.*, **129**, 2861–2883, doi:10.1175/1520-0493(2001)129<2861:RTMSMF>2.0.CO;2.
- Kubota, T., and Coauthors, 2007: Global precipitation map using satellite-borne microwave radiometers by the GSMaP project: Production and validation. *IEEE Trans. Geosci. Remote Sens.*, **45**, 2259–2275, doi:10.1109/TGRS.2007.895337.
- Li, Q., R. Ferraro, and N. Grody, 1998: Global distribution of SSM/I rainfall retrieval error. Preprints, *Ninth Conf. on Satellite Meteorology*, Vol. 2, Paris, France, Amer. Meteor. Soc., 639–642.
- Lin, Y., and K. E. Mitchell, 2005: The NCEP stage II/IV hourly precipitation analyses: Development and applications. *19th Conf. on Hydrology*, Amer. Meteor. Soc., San Diego, CA, 1.2. [Available online at <https://ams.confex.com/ams/Annual2005/webprogram/Paper83847.html>.]
- McCollum, J. R., W. F. Krajewski, R. R. Ferraro, and M. B. Ba, 2002: Evaluation of biases of satellite rainfall estimation algorithms over the continental United States. *J. Appl. Meteor.*, **41**, 1065–1080, doi:10.1175/1520-0450(2002)041<1065:EOBOSR>2.0.CO;2.
- Miller, S. W., P. A. Arkin, and R. Joyce, 2001: A combined microwave/infrared rain rate algorithm. *Int. J. Remote Sens.*, **22**, 3285–3307, doi:10.1080/01431160152609155.
- Tan, P. N., M. Steinbach, and V. Kumar, 2005: *Introduction to Data Mining*. Addison-Wesley, 769 pp.
- Turk, F. J., G. Rohaly, J. Hawkins, E. A. Smith, F. S. Marzano, A. Mugnai, and V. Levizzani, 2000: Meteorological applications of precipitation estimation from combined SSM/I, TRMM and geostationary satellite data. *Microwave Radiometry and Remote Sensing of the Earth's Surface and Atmosphere*, P. Pampaloni and S. Paloscia, Eds., VSP, 353–364.
- Vila, D., C. Hernandez, R. Ferraro, and H. Semunegus, 2013: The performance of hydrological monthly products using SSM/I–SSMIS sensors. *J. Hydrometeorol.*, **14**, 266–274, doi:10.1175/JHM-D-12-056.1.

- Wolff, D. B., and B. L. Fisher, 2009: Assessing the relative performance of microwave-based satellite rain-rate retrievals using TRMM ground validation data. *J. Appl. Meteor. Climatol.*, **48**, 1069–1099, doi:[10.1175/2008JAMC2127.1](https://doi.org/10.1175/2008JAMC2127.1).
- Xie, P., and P. A. Arkin, 1997: Global precipitation: A 17-year monthly analysis based on gauge observations, satellite estimates, and numerical model outputs. *Bull. Amer. Meteor. Soc.*, **78**, 2539–2558, doi:[10.1175/1520-0477\(1997\)078<2539:GPAYMA>2.0.CO;2](https://doi.org/10.1175/1520-0477(1997)078<2539:GPAYMA>2.0.CO;2).
- , ——, and J. E. Janowiak, 2007: CMAP: The CPC merged analysis of precipitation. *Measuring Precipitation from Space*, V. Levizzani, P. Bauer, and F. J. Turk, Eds., Springer, 319–328.
- Yin, Z.-Y., X. Zhang, X. Liu, M. Colella, and X. Chen, 2008: An assessment of the biases of satellite rainfall estimates over the Tibetan Plateau and correction methods based on topographic analysis. *J. Hydrometeorol.*, **9**, 301–326, doi:[10.1175/2007JHM903.1](https://doi.org/10.1175/2007JHM903.1).